A NEW LOOK AT THE TOPOGRAPHY OF THE SOUTH POLE WITH LOLA. M. K. Barker[1], Erwan Mazarico[1], Gregory A. Neumann[1], David E. Smith[2], Maria T. Zuber[2] and James W. Head[3], [1]NASA Goddard Space Flight Center, Greenbelt, MD 20771, USA, [2]Department of Earth, Atmospheric, and Planetary Sciences, MIT, Cambridge, MA, 02139, USA, [3]Department of Earth, Environmental and Planetary Sciences, Brown University, Providence, RI 02912, USA

Introduction: The lunar south polar region is a high priority target for scientific investigation (NASEM, 2022). Many robotic and human missions are planned for the south pole over the next decade including NASA's Artemis III scheduled for launch in 2025. Precise and accurate topographic maps are critical inputs to many aspects of the design of these missions, such as locating volatile cold traps, traverse planning, optimizing power and communications assets, and terrain relative navigation [2]. We need to know the topography both outside and within permanently shadowed regions (PSRs) on lander-relevant scales. Imaging-based techniques, like stereo-photogrammetry and shape-from-shading, face challenges in the polar regions due to the extreme lighting and shadowing conditions found there. Laser altimeters like the Lunar Orbiter Laser Altimeter (LOLA) on the Lunar Reconnaissance Orbiter (LRO) can see into the shadows given their active ranging capabilities, but gaps between ground tracks and individual laser spots require interpolation and lead to uncertainties in the resulting digital elevation models (DEMs). Also, small errors in the spacecraft orbit reconstruction (typically a few meters horizontally and ~0.5 m vertically for LRO) can cause streaky artifacts in a LOLA-based DEM (LDEM) at the very high resolutions necessary for lander and site planning studies.

To address these issues, we previously derived new 5 m/pix LDEMs for several south polar sites, selected for their high average solar illumination [3]. More recently, we have been applying those techniques to make new LDEMs over larger areas and at multiple pixel scales spanning 10 m/pix to 240 m/pix. From these new and improved LDEMs, we are also making new derived products, such as a 20 m/px PSR map and roughness maps over the 80 – 90° S region. The new LDEMs and derived products will be publicly released in the near future. Here we present preliminary results and interpretations.

New LDEMs: We divide the 80 – 90° S region into 64 tiles with a pixel scale of 20 m/pix. Each tile is 80 km on a side with 2 km overlaps between tiles. The track adjustment and cleaning process is run on each tile independently following the methods in [3]. In summary, for each tile, we randomly remove 2% of the tracks from the LDEM and adjust each of the missing tracks individually to the resulting "reduced" LDEM. This adjustment involves applying 3-dimensional (3-D) offsets and minimizing the root-mean-squared (RMS) surface height residuals between each individual laser return and the surface height at that location on the current reduced LDEM. This step is repeated until all tracks have been adjusted. The process of running 50 batches until all tracks are adjusted is repeated 5 times in total, each time starting from a new LDEM computed with the best-fit track adjustments from the previous iteration. Outlying points are down-weighted during the track fitting to ensure they do not bias the results, and are removed after the final iteration.

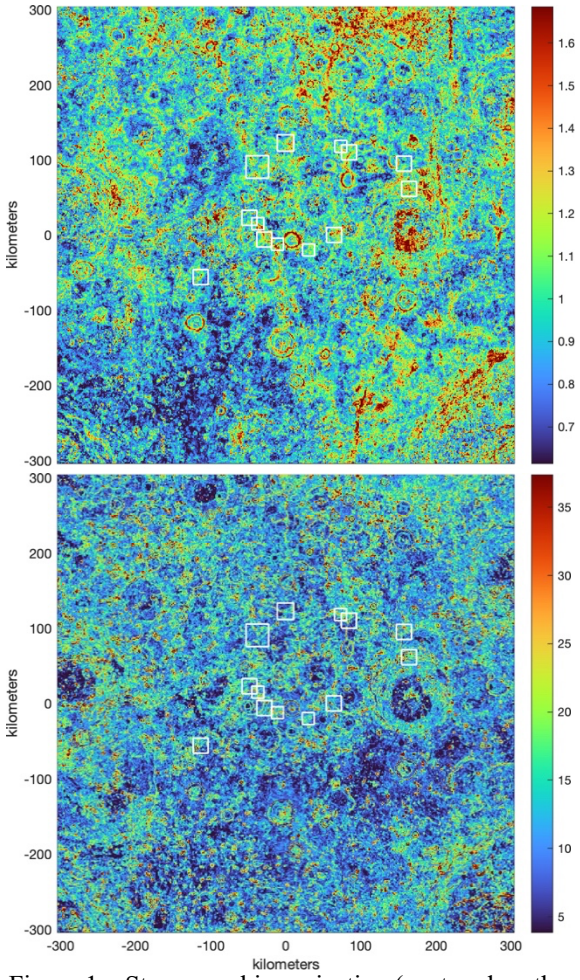

Figure 1 – Stereographic projection (centered on the south pole) of LOLA roughness on baselines of 200 m (top) and 1600 m (bottom). The color scale ranges from the 2nd to the 98th percentile (in meters). White squares outline the 13 candidate Artemis III sites.

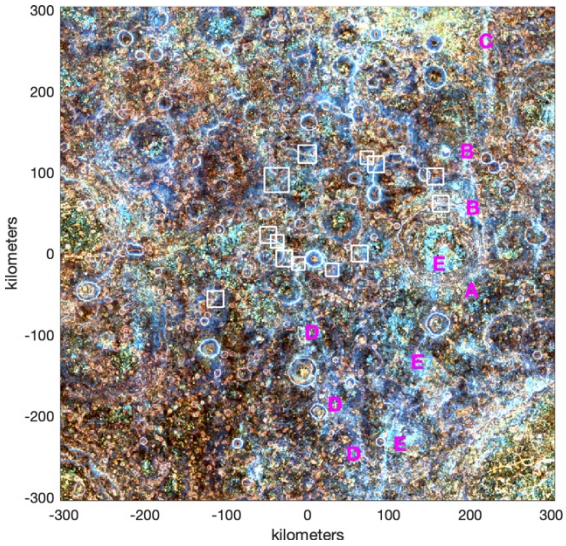

Figure 2 – Color composite image of LOLA roughness with each baseline assigned to a different color: 50 m (blue), 100 m (teal), 200 m (cyan), 400 m (yellow), 800 m (orange) and 1600 m (red).

The cleaned tile point clouds are individually aligned to the original LDEM with a rigid 3-D translation using the Ames Stereo Pipeline's *pc_align* tool [4]. The aligned point clouds are then gridded using the natural neighbor method [5] and blended together with a cosine taper weight in the overlap regions using the Generic Mapping Tools *grdblend* utility [6].

Roughness: Terrain roughness is a useful probe of geologic processes on and below the surface over a wide range of horizontal scales [e.g., 7-11]. Therefore, it can provide valuable information for scientific and exploration studies. To that end, we take a fresh look at the south polar regional roughness characteristics using the newly adjusted LOLA point cloud and LDEM.

We make roughness maps by computing a slope-detrended and outlier-resistant standard deviation of height residuals. Specifically, we fit a plane to the 20 m/pix LDEM within different radii (half the baseline) and compute the standard deviation as 1.48 times the median absolute deviation of the height residuals of the LOLA spots relative to the plane. Figure 1 shows two examples. It is also helpful to visualize all the roughness maps combined into a color composite image (Figure 2). A strong intensity of a particular color signifies a relatively high roughness at the corresponding baseline.

These maps reveal a diversity of terrains characterized by their roughness. Some areas, such as the floors of Amundsen and Newton A (-108 km, 283 km), appear blue-to-cyan in the color composite signifying a pronounced increase in roughness at baselines < 400 m relative to 800 – 1600 m. These regions are relatively heavily populated with craters of diameter < 400 m, which are too small to appear in the 1600 m slope and roughness maps and thus they are relatively flat and smooth at the longest baseline.

Several linear features are apparent running predominantly up-down (in plan view). These are most visible at baselines < 400 m with shades of blue to cyan in the color composite. The thinnest of these (A – C in Figure 2) have widths < 5 km and may be examples of the "roughness rays and lineaments" previously identified at lower latitudes in global hectometer-scale roughness maps [8]. Such features may be chains of secondary craters although they are not always associated with large (>20 km) craters [8].

There is also tentative evidence for two more diffuse, longer, and wider swaths (D and E) of variably high roughness on short baselines. Swath D may be part of a Tycho ejecta ray visible in maps of LRO Wide Angle Camera UV reflectance and LOLA 1064 nm normal albedo [12]. A great circle through swath E passes close to a linear reflectance feature and several large craters (Antoniadi, Crookes, and Jackson) equatorward of 80° S. If E is another ejecta ray, then that could explain why Amundsen's floor is so rough (~90th percentile) at short (≤ 400 m) baselines compared to other large craters, like Shoemaker, Schrödinger, and Drygalski (-317 km, 16 km). The large flat floors of these craters are relatively immune to the smaller-scale crater-erasing effects of mass wasting, but only Amundsen experienced the bombardment of secondary impactors responsible for swath E. Nonuniformities in swath width and roughness could reflect variations in density of secondary impactors and/or target terrain properties.

References: [1] Nat. Acad. of Sci., Eng., and Med., 2022, Wash., DC: The Nat. Acad. Press. DOI: 10.17226/26522. [2] Heldmann, J. L., et al., 2016, Acta Astron., 127, 308. DOI: 10.1016/j.actaastro.2016.06.014. [3] Barker, M. K., et al., 2021, Planet. and Sp. Sci., 203, 105119. DOI: 10.1016/j.pss.2020.105119. [4] Beyer, R. A., et al., 2018, Earth and Sp. Sci., 5, 9. DOI: 10.1029/2018EA000409. [5] Sibson, R., 1981, In Interpolating multivariate data, New York: John Wiley & Sons, pp. 21-36. [6] Wessel, P., et al., 2013, EOS Trans. AGU, 94, 409. DOI: 10.1002/2013EO450001. [7] Deutsch, A., et al., 2021, PSJ, 2, 213. DOI: 10.3847/PSJ/ac24ff. [8] Kreslavsky, M. A., et al., 2013, Icarus, 226, 52. DOI: 10.1016/j.icarus.2013.04.027. [9] Wang, J., et al., 2020, JGRE, 125, 10, e06091. DOI: 10.1029/2019JE006091. [10] Cai, Y. & Fa, W., 2020, JGRE, 125, 8. DOI: 10.1029/2020JE006429. [11] Hayne, P. O., et al., 2021, Nature Astro., 5, 169. DOI: 10.1038/s41550-020-1198-9. [12] Bernhardt H., et al., 2022, Icarus, 379, 114963. DOI: 10.1016/j.icarus.2022.114963.